

Crystal Structure of the Metallo- β -Lactamase GOB in the Periplasmic Dizinc Form Reveals an Unusual Metal Site

Jorgelina Morán-Barrio,^a María-Natalia Lisa,^{a,b} Nicole Larrieux,^b Salvador I. Drusin,^{c,d} Alejandro M. Viale,^a Diego M. Moreno,^{c,e} Alejandro Buschiazzo,^{b,f} Alejandro J. Vila^a

Departamento de Química Biológica and Instituto de Biología Molecular y Celular de Rosario (IBR, CONICET-UNR), Facultad de Ciencias Bioquímicas y Farmacéuticas, Universidad Nacional de Rosario, Rosario, Argentina^a; Laboratory of Molecular & Structural Microbiology, Institut Pasteur de Montevideo, Montevideo, Uruguay^b; Departamento de Química-Física, Facultad de Ciencias Bioquímicas y Farmacéuticas, Universidad Nacional de Rosario, Rosario, Santa Fe, Argentina^c; Instituto de Biología Molecular y Celular de Rosario (CONICET-UNR), Ocampo y Esmeralda, Rosario, Argentina^d; Instituto de Química de Rosario (QUIR, CONICET-UNR), Rosario, Santa Fe, Argentina^e; Département de Biologie Structurale et Chimie, Institut Pasteur, Paris, France^f

Metallo-beta-lactamases (MBLs) are broad-spectrum, Zn(II)-dependent lactamases able to confer resistance to virtually every β -lactam antibiotic currently available. The large diversity of active-site structures and metal content among MBLs from different sources has limited the design of a pan-MBL inhibitor. GOB-18 is a divergent MBL from subclass B3 that is expressed by the opportunistic Gram-negative pathogen *Elizabethkingia meningoseptica*. This MBL is atypical, since several residues conserved in B3 enzymes (such as a metal ligand His) are substituted in GOB enzymes. Here, we report the crystal structure of the periplasmic di-Zn(II) form of GOB-18. This enzyme displays a unique active-site structure, with residue Gln116 coordinating the Zn1 ion through its terminal amide moiety, replacing a ubiquitous His residue. This situation contrasts with that of B2 MBLs, where an equivalent His116Asn substitution leads to a di-Zn(II) inactive species. Instead, both the mono- and di-Zn(II) forms of GOB-18 are active against penicillins, cephalosporins, and carbapenems. *In silico* docking and molecular dynamics simulations indicate that residue Met221 is not involved in substrate binding, in contrast to Ser221, which otherwise is conserved in most B3 enzymes. These distinctive features are conserved in recently reported GOB orthologues in environmental bacteria. These findings provide valuable information for inhibitor design and also posit that GOB enzymes have alternative functions.

The expression of β -lactamases is the main mechanism of bacterial resistance against β -lactam antibiotics. These enzymes catalyze the hydrolysis of the amide bond in the β -lactam ring characteristic of this family of drugs (1–5). MBLs are metal-dependent hydrolases which generally use Zn(II) as a Lewis acid to activate a water molecule for the nucleophilic attack. These enzymes are refractive to clinically employed lactamase inhibitors (1) and have a particular relevance in the clinical setting as they can hydrolyze a broad spectrum of β -lactam substrates, being able to inactivate carbapenems, the “last-resort” antibiotics in antibacterial therapy (6).

MBLs have been classified into subclasses B1, B2, and B3 based on sequence identity (7). Crystal structures of MBLs from the three subclasses have revealed that these enzymes present a common $\alpha\beta/\beta\alpha$ sandwich fold, with the active site located within a groove at the interface between these two halves (1–6). The Zn(II)-binding residues vary among different subclasses, giving rise to diverse metal site architectures and metal contents required for activity (1–6). B1 and B3 MBLs are broad-spectrum enzymes that hydrolyze penicillins, cephalosporins, and carbapenems with a wide variety of *in vitro* catalytic efficiencies, displaying a broad range of resistance profiles *in vivo* (1–5, 8). The di-Zn(II) form of B1 MBLs has been shown to be the active form in the bacterial periplasm, despite contradictory data obtained from *in vitro* studies (8–10). These enzymes display a conserved metal binding motif, where the coordination sphere of the metal ion in the Zn1 site involves three His residues (3-H site), His116, His118, and His196, and a water/hydroxide molecule (the active nucleophile) in a tetrahedral arrangement, while the metal ion in the Zn2 site adopts a trigonal bipyramidal coordination sphere, with Asp120, Cys221, His263 (DCH site), a water molecule, and the formerly

mentioned water/hydroxide molecule as ligands (11–15) (Fig. 1). Instead, B2 MBLs are essentially exclusive carbapenemases and are active with one Zn(II) ion bound to the Zn2 site (superimposable to the B1 DCH site), while binding of a second metal equivalent to the Zn1 site results in enzyme inhibition (16, 17). Substitution His116Asn (present in all B2 enzymes) impairs metal binding to the Zn1 site by removing a metal ligand. Consequently, nucleophile activation does not involve a metal ion (16, 18, 19). B3 lactamases, distantly related to the B1 and B2 subclasses, are mostly di-Zn(II) enzymes (20–24). The Zn1 site of B3 enzymes is a 3-H site similar to that of B1 enzymes, whereas two mutations (Cys221Ser and Arg121His) affect the Zn2 coordination geometry (20–24), and the metal ion is bonded to Asp120, His121, and His263. Ultimately, Ser221 (equivalent to Cys221 in the DCH site) is no longer a metal ligand, so that the Zn2 site is a DHH site in B3 MBLs. In addition, a third water molecule participates as a fifth

Received 24 May 2016 Returned for modification 5 July 2016

Accepted 17 July 2016

Accepted manuscript posted online 25 July 2016

Citation Morán-Barrio J, Lisa M-N, Larrieux N, Drusin SI, Viale AM, Moreno DM, Buschiazzo A, Vila AJ. 2016. Crystal structure of the metallo- β -lactamase GOB in the periplasmic dizinc form reveals an unusual metal site. *Antimicrob Agents Chemother* 60:6013–6022. doi:10.1128/AAC.01067-16.

Address correspondence to Alejandro J. Vila, vila@ibr-conicet.gov.ar, or Alejandro Buschiazzo, alebus@pasteur.edu.uy.

J.M.-B. and M.-N.L. contributed equally to this work.

Supplemental material for this article may be found at <http://dx.doi.org/10.1128/AAC.01067-16>.

Copyright © 2016, American Society for Microbiology. All Rights Reserved.

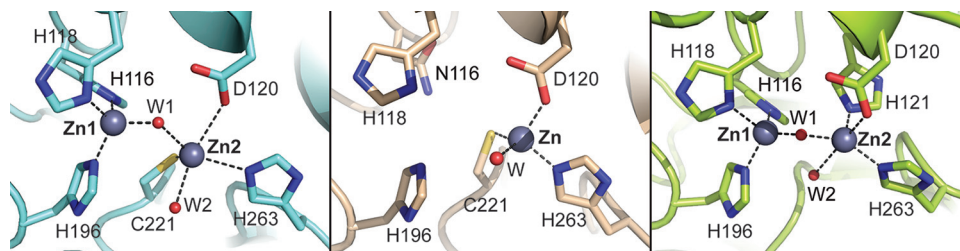


FIG 1 Metallo-beta-lactamase zinc-binding sites. *B. cereus* BcII (B1; PDB entry 1BC2) (left), *S. fonticola* SfhI (B2; PDB entry 3SD9) (center), and *S. maltophilia* L1 (B3; PDB entry 1SML) (right) are shown. Zinc atoms are shown as gray spheres, and water molecules (W) are shown as small red spheres. Coordination bonds are indicated with dashed lines.

ligand, giving rise to a square pyramidal coordination sphere of Zn2 (20–24). Similar to B1 enzymes, the Zn1 ion in B3 lactamases is regarded as responsible for nucleophile activation (20–24).

The deepest branching member of the MBL B3 subclass, GOB from *Elizabethkingia meningoseptica* (formerly *Chryseobacterium meningosepticum*), presents several unusual features. Despite being related to B3 lactamases based on sequence homology, GOB enzymes present a His116Gln substitution that resembles the active-site mutation found in B2 enzymes (25). In addition, Ser221 is replaced by a Met residue, suggesting a more divergent metal binding site or a B2–B3 hybrid enzyme. GOB-type enzymes include 18 allelic variants, all of them expressed by *E. meningoseptica*, a pathogen responsible for neonatal meningitis and opportunistic infections in immunocompromised patients (26–28). So far, two GOB variants have been characterized biochemically, GOB-1 and GOB-18 (29–32), which differ by three residues located far from the active site (29). Expression of GOB-1 in the periplasm of *Escherichia coli* led to a di-Zn(II) enzyme showing a broad substrate profile similar to most B3 MBLs (30). Instead, cytoplasmic expression of GOB-18 resulted in accumulation of a nonactive Fe(III)-substituted form. This variant, with metal depleted and reconstituted with Zn(II), was able to bind only one metal equivalent in the putative DHH site, as confirmed by mutagenesis and spectroscopic studies (29). Mono-Zn(II)-GOB-18 behaved as a fully active, broad-spectrum B3 enzyme. These data, together with the unusual residues present in positions 116 and 221, suggested that GOB enzymes have novel structural and functional features.

Here, we report the crystal structure of the periplasmic form of GOB-18, which shows that GOB enzymes are unique among MBLs. GOB-18 contains a dinuclear Zn(II) site, revealing that replacement of His116 does not preclude these lactamases from binding two metal ions. Indeed, Gln116 is a metal ligand in the Zn1 site, resulting in a novel HQH site instead of the canonical 3-H site. Met221 (yet another singularity of GOB enzymes) is not a metal ligand and is not involved in substrate binding, further confirmed by docking and molecular dynamics simulations. Thus, GOB enzymes present a divergent metal binding site with novel substrate binding features which make them unique among B3 MBLs. This observation, together with the finding that the resistance profile of *E. meningoseptica* is elicited mostly by the B1 enzyme BlaB (33), discloses a functional redundancy and suggests that GOB enzymes play alternative roles in this microorganism that have yet to be disclosed.

MATERIALS AND METHODS

Chemicals. Biochemical reagents were purchased from Sigma-Aldrich except when specified otherwise. Molecular biology reagents were purchased from Promega, Invitrogen, or New England BioLabs. Metal-free buffers were prepared by adding Chelex 100 to normal buffers and stirring for 0.5 h.

Production of recombinant GOB-18 in the periplasmic space of *E. coli*. GOB-18 was produced in the periplasmic space of *E. coli* C41(DE3) cells harboring the plasmid pKP-GOB-18 (29, 31, 32). This vector allows the production of recombinant GOB-18 as a C-terminal fusion to the leader peptide *pelB* (29, 31). Secretion via the Sec pathway allows processing of the precursor and targeting the mature protein to the periplasmic space of the bacterial host. *E. coli* C41(DE3) cells harboring plasmid pKP-GOB-18 were grown aerobically at 30°C in LB broth supplemented with kanamycin (50 µg/ml) until reaching 0.6 U of absorbance at 600 nm. Protein production was induced by adding isopropyl β-D-1-thiogalactopyranoside (IPTG) to a final concentration of 1 mM, and the incubation was continued for 16 h at the same temperature. Mature GOB-18 was extracted from the cellular periplasm by a two-step osmotic shock procedure without lysozyme or EDTA. Briefly, cells were harvested and resuspended with 1 ml/g (wet weight) of 20 mM Tris-HCl, pH 8, 50% (wt/vol) sucrose, 0.1 mM phenylmethylsulfonyl fluoride, and incubated for 2 h at 4°C under orbital shaking. Ten milliliters of ice-cold water were added per milliliter of suspension and further incubated for 2 h under the same conditions. After centrifugation at 15,000 × g for 8 min at 4°C, the supernatant (first extract) was collected and stored at 4°C. The pellet was further resuspended in ice-cold water in half the volume used for the first extract and incubated under the same conditions for 1.5 h at 4°C. The supernatant (second extract) was collected and pooled with the first one, rendering the periplasmic fraction.

Purification of GOB-18 from the periplasmic fraction of *E. coli*. Mature GOB-18 was purified to homogeneity with two steps of ionic exchange chromatography (Fig. 2). The periplasmic extract was adjusted to pH 7 and loaded onto a Sephadex CM-50 column (Sigma) preequilibrated with buffer E (20 mM Tris-HCl, pH 7). The resin was washed with 5 column volumes of buffer E and eluted with buffer E supplemented with 400 mM NaCl. The elution peak was concentrated, dialyzed against buffer E, and loaded onto a Mono S column (GE Healthcare) preequilibrated with buffer E. Elution was achieved with buffer E with added NaCl (gradient of 0 to 1 M). Samples containing GOB-18 were pooled and concentrated to 20 mg/ml, frozen in liquid nitrogen, and stored at –70°C until crystallography assays. An aliquot of the enzyme was stored at 4°C for kinetic analyses. The average purification yields obtained were ca. 1 mg of GOB-18 per liter of *E. coli* culture, resulting in the expected 31-kDa polypeptide, as estimated by SDS-PAGE.

Metal content determination. The metal content of purified GOB-18 was measured by atomic absorption spectroscopy in a Metrolab 250 instrument operating in flame mode.

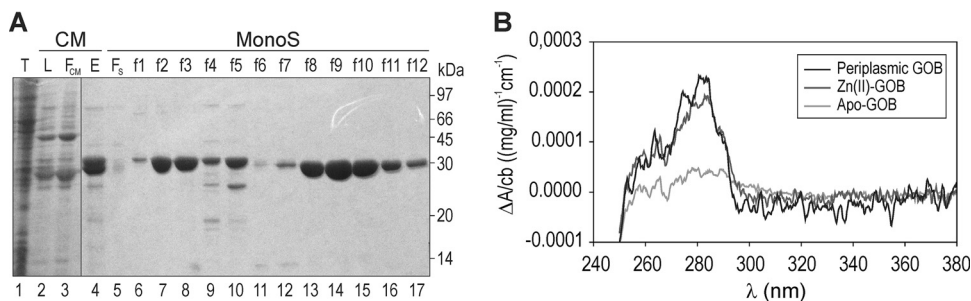


FIG 2 Purification and characterization of periplasmic GOB-18. (A) SDS-PAGE analysis of fractions along different steps of the purification process. Lanes: 1, total cell extract (T); 2, periplasmic fraction corresponding to the sample loaded on the CM-Sephadex column (L); 3, CM-Sephadex flowthrough (F_{CM}); 4, CM-Sephadex elution, corresponding to the sample loaded on the Mono S column (E); 5, Mono S flowthrough (F_S); 6 to 17, Mono S elution fractions (f1 to f12). Molecular mass markers (in kilodaltons) are indicated at the right. The vertical gray line between lanes 3 and 4 indicates the junction of two different gels prepared and run together, since the Mini Protean III system (Bio-Rad) holds up to 15 lanes. (B) Circular dichroism spectra of periplasmic GOB-18 (black line), remetalated Zn(II)-GOB-18 (gray), and apo-GOB-18 (light gray). $\Delta A/cb$ is the molar ellipticity, where c is the protein concentration in mg/ml and b is the path length in cm.

Circular dichroism spectroscopy. The circular dichroism spectrum of periplasmic GOB-18 was obtained using a JASCO J-810 spectropolarimeter at 25°C.

Determination of the kinetic parameters. Antibiotic hydrolysis was monitored by absorbance variation resulting from the scission of the β -lactam ring. Reactions were performed in 15 mM HEPES, pH 7.5, 200 mM NaCl at 30°C. The kinetic parameters K_m and k_{cat} were derived from initial rate measurements, as recorded with a Jasco V-550 spectrophotometer, and were estimated by nonlinear data fitting to the integrated form of the Michaelis-Menten equation.

Crystallization and data collection. Crystals grew from a 9.8 mg/ml solution of GOB-18 by adding 0.5 μ l of protein to 1.5 μ l mother liquor [100 mM Tris-HCl, pH 8.5, 1.7 M NaCl, 1.7 M $(NH_4)_2SO_4$] in a hanging-drop setup with 1 ml mother liquor in the reservoir. These were not single crystals, which were eventually obtained by microseeding fresh drops under identical conditions except for using a slightly modified mother liquor [2 M NaCl/ $(NH_4)_2SO_4$ and avoiding Tris-HCl]. Single crystals reached a size of ca. 150 μ m and were cryoprotected in mother liquor containing 25% glycerol and flash frozen in liquid nitrogen. X-ray diffraction data were collected in-house (Unit of Protein Crystallography, Institut Pasteur de Montevideo, Montevideo, Uruguay) from a single crystal with a MicroMax-007 HF X-ray source (Rigaku) and a MAR345 image plate detector (Mar Research), employing radiation of 1.5418 Å. The diffraction data were processed using XDS (34) and scaled with Aimless (35) from the CCP4 program suite.

Structure determination and refinement. The crystal structure of GOB-18 was solved by molecular replacement using the program Phaser (36) and the model of native FEZ-1 from *Legionella gormanii* (PDB entry 1K07) as a search probe. The asymmetric unit contains two monomers of GOB-18 (chains A and B) with ca. 44% of the volume occupied by solvent. SigmaA-weighted Fourier maps (2mFo-DFc) allowed rebuilding the initial model reliably through iterative cycles of manual model building with COOT (37) and refinement with BUSTER (38). To minimize model bias, initial refinement cycles were carried out, including high-temperature (7,500K), slow-cooling simulated annealing procedures, in torsional space (as implemented in the program PHENIX [39]). The final model revealed two outlier residues in the Ramachandran plot. Figures were generated and rendered with PyMOL 1.5.0.2. (Schrödinger, LLC). Volume calculations for automatically identified cavities were done using the CASTp algorithm (40) and Q-site finder (41), giving similar results.

Substrate docking and molecular dynamics simulations. Molecular docking was performed using Autodock 4.2 (42). Deprotonated imipenem was docked using a docking box of 40 by 40 by 40 Å (grid-point spacing of 0.375 Å) centered in the enzyme active site. The model of GOB-imipenem was built *in silico* by making a structural alignment with

the structure of L1-imipenem using the Multiseq plug-in of VMD (43). Molecular dynamics simulations were performed starting from the complexes GOB-18-imipenem and L1-imipenem. Each complex was immersed in a truncated octahedral periodic box with a minimum solute-wall distance of 8 Å and filled with explicit TIP3P water molecules (44). Molecular dynamic simulations were performed with the AMBER14 package (45, 46) using ff14SB (47). Particle-mesh Ewald (PME) was implemented for long-range interactions with a cutoff distance of 12 Å (48). Temperature and pressure were regulated with the Berendsen thermostat and barostat (49). All bonds involving hydrogen were fixed using the SHAKE algorithm (50). Each initial system was equilibrated at 300K using a conventional protocol and then subjected to 50 ns of simulation in the NVT ensemble. To maintain the coordination environment around zinc atoms, we used harmonic bonds between the metal centers and the residues of the coordination sphere. We applied a restraint to keep the imipenem bound to the active site. Calculations of the root mean squared deviations (RMSD) and root mean square fluctuations (RMSF) of the molecular dynamics simulations were performed using the cpptraj module of AMBER (51).

Accession number. Atomic coordinates and structure factors were deposited in the Protein Data Bank under accession code 5K0W.

RESULTS

Expression and purification of GOB-18 for crystallogensis.

Production of GOB-18 in *E. coli* gives rise to different metallated species depending on the cellular compartment where the protein accumulates. Overexpression of GOB-18 in the cytoplasm results in an inactive Fe(III)-bound form, from which a mononuclear fully active Zn(II) variant can be prepared by metal chelation and remetalation *in vitro* (29). Instead, GOB exclusively binds Zn(II) when it is secreted into the bacterial periplasm (29, 31).

GOB-18 produced in the cytoplasm of *E. coli*, both the Fe(III)-containing variant and the reconstituted mono-Zn(II) form, proved recalcitrant after extensive crystallization trials. Thus, an alternative protocol was optimized, allowing the production of GOB-18 in the bacterial periplasm, which is the physiological cellular compartment for MBLs' expression in Gram-negative species (Fig. 2A). This strategy yielded GOB-18 containing exclusively Zn(II), with a maximum metal content of (1.4 ± 0.1) Zn(II) equivalents/GOB-18 molecule as determined by atomic absorption spectroscopy. This metal content figure indicates the presence of a dinuclear GOB-18 species, which is consistent with previous reports for GOB-1 (30). Circular dichroism of periplasmic GOB-18

TABLE 1 Kinetic parameters of hydrolysis of β -lactam substrates by GOB enzymes^c

Substrate and concn of Zn(II) added (μM)	GOB-18						GOB-1 ^b		
	Periplasmic			Cytoplasmic ^a			k_{cat} (s^{-1})	K_m (μM)	k_{cat}/K_m ($\text{s}^{-1} \mu\text{M}$)
Imipenem									
0	37 \pm 1	22 \pm 3	1.7 \pm 0.5	42 \pm 9	26 \pm 2	1.6 \pm 1.5	77 \pm 2	18 \pm 0.6	4.2
20	75 \pm 3	42 \pm 7	1.8 \pm 0.5						
50							85 \pm 2	13 \pm 1	6.5
Meropenem									
0	96 \pm 4	54.3 \pm 6	1.8 \pm 0.6	72 \pm 0.5	40 \pm 10	1.8 \pm 0.5	100 \pm 7	29 \pm 1	3.5
20	261 \pm 9	170 \pm 20	1.5 \pm 0.7						
50							170 \pm 3	22 \pm 1	8.0
Cefaloridine									
0	41 \pm 2	100 \pm 10	0.4 \pm 0.1	30 \pm 2	31 \pm 0.5	0.95 \pm 0.08			
20	59 \pm 2	150 \pm 20	0.4 \pm 0.1						
Cefotaxime									
0	80 \pm 3	100 \pm 10	0.8 \pm 0.3	83 \pm 2	88 \pm 6	0.94 \pm 0.09			
20	106 \pm 5	130 \pm 20	0.8 \pm 0.3						
Penicillin G									
0	1,070 \pm 20	450 \pm 20	2.4 \pm 0.9	680 \pm 80	330 \pm 30	2.1 \pm 0.4	540 \pm 7	130 \pm 6	4.2
20	1,810 \pm 40	580 \pm 50	3.1 \pm 0.9						
50							630 \pm 10	190 \pm 10	3.4

^a Values correspond to mono-Zn(II)-GOB from reference 29.

^b Values correspond to reference 30.

^c Values were derived from a nonlinear fit of the Michaelis-Menten equation to initial rate measurements and correspond to the averages from at least three independent enzyme preparations.

indicates it has a tertiary structure similar to that of the *in vitro* reconstituted Zn(II) form (29) (Fig. 2B). Periplasmic GOB-18 was able to catalyze the hydrolysis of a broad spectrum of β -lactam substrates, with k_{cat} and K_m values similar to those formerly reported for mono-Zn(II) and di-Zn(II)-GOB-1 and with no changes in the catalytic efficiencies upon addition of 20 μM Zn(II) to the reaction medium (Table 1). Nevertheless, in contrast to reconstituted Zn(II)-GOB-18, periplasmic GOB-18 crystallized under different conditions containing high concentrations of NaCl and $(\text{NH}_4)_2\text{SO}_4$ as precipitants.

Crystal structure of periplasmic GOB-18. Periplasmic GOB-18 crystallized in space group P2₁, with crystals diffracting X rays to 2.6-Å resolution (Table 2). The final refined atomic model contains two protein molecules per asymmetric unit, 4 zinc atoms, 8 chloride atoms, 77 water molecules, and one glycerol molecule. The two protein chains are very similar, with an RMSD of 0.26 Å among 266 aligned α -carbons. Chain A includes residues Ser17 to Asp286 (the side chains of residues Asn26 and Asp286 were not included in the model due to weak electron density), while monomer B spans residues Val20 to Lys290 (similarly, the Val20 side chain was not modeled), with a continuous main-chain trace throughout. GOB-18 displays the expected $\alpha\beta/\beta\alpha$ sandwich fold, with two core β -sheets composed of 7 (β 1 to β 7) and 5 (β 8 to β 12) β -strands, respectively, and 6 α -helices (Fig. 3A). Helices α 1 to α 4 cover the 7-stranded β -sheet, with helix α 4 closing one side of the metal-binding groove. On the other hand, helices α 5 and α 6 wrap around the 5-stranded β -sheet, with the intervening region β 12- α 6, including three short helical elements, closing up the other side of the catalytic site. As already described for the MBL fold

(1–6), the whole domain of GOB-18 can be depicted as a duplication of two structurally similar α/β hemidomains.

GOB-18 is very similar to other B3 lactamases (20–24), despite low sequence identity. Structural alignment of GOB-18 (chain A) with available B3 lactamase models allows for similarity quantification (Fig. 3B) for FEZ-1 (PDB entry 1K07; 1.27 Å RMSD for 243 aligned residues), BJP-1 (PDB entry 3LVZ; 1.50 Å RMSD for 239 residues), and L1 (PDB entry 1SML; 1.55 Å RMSD for 236 residues). When calculated per residue, the largest local RMSD values are observed for two loops flanking the active site, which are expected to be involved in substrate specificity: loop 1 (residues 130 to 152 in GOB-18, equivalent to 148 to 172 according to BBL numbering; to facilitate comparative analyses, residue numbering here will be stated for GOB-18 followed by BBL numbering in parenthesis) and loop 2 (residues 198 to 218 [219 to 239]). Structural differences are also noticeable in the β 12- α 6 loop (residues 239 to 265 [261 to 287]) as well as in the N terminus of the protein.

All B3 lactamases crystallized so far are characterized by at least one disulfide bridge, in most cases between Cys residues located in the C-terminal helix and the loop linking elements α 5 and β 12 (20–24). GOB-18 is an exception in this regard within B3 enzymes, with only one Cys residue in its primary structure, i.e., Cys180 (201) (in strand β 10), which is buried within the protein core (Fig. 3A) forming hydrogen bonds in the base of the metal binding site (see below).

Active site of di-Zn(II)-GOB-18. The electron density maps revealed the presence of two heavy atoms in the active sites of each GOB-18 monomer in the asymmetric unit (Fig. 4A). They occupy the metal binding sites found in other dinuclear MBLs and can be

TABLE 2 X-ray diffraction data collection and refinement statistics

Parameter ^b	Value(s) for GOB-18 ^a
Data collection statistics	
Space group	P2 ₁
Protein molecules per asymmetric unit (no.)	2
Solvent content (%)	43.9
Wavelength (Å)	1.5418
Data resolution (Å)	24.33–2.61 (2.75–2.61)
Measured reflections (no.)	44,417
Multiplicity	2.8 (2.6)
Completeness (%)	96.9 (90.5)
R _{meas} (%)	15.1 (45.3)
<I/σ(I)>	9.5 (3.3)
Unit cell dimensions	
a, b, c (Å)	64.0, 48.5, 88.9
β (°)	100.1
Refinement statistics	
Resolution range (Å)	24.3–2.61
R _{cryst} (no. of reflections)	0.192 (15,152)
R _{free} (no. of reflections)	0.242 (955)
RMSD	
Bond length (Å)	0.01
Bond angle (degrees)	1.11
No. of atoms/molecules	
Protein nonhydrogen	4,381
Water	77
Zn ⁺²	4
Glycerol	6
Cl ⁻¹	8
Mean B factor (Å ²)	
Overall (chain A/chain B)	28/31
Main chain (chain A/chain B)	25/27
Side chains (chain A/chain B)	32/35
Waters	18
Liganded Zn ⁺²	28
Liganded Cl ⁻¹	47
Liganded glycerol	41
Map vs model correlation coefficient ^c (overall/local)	0.839/0.881
No. of residues in Ramachandran plot regions ^d (allowed/favored/outliers)	535/524/2
PDB entry	5K0W

^a Values in parentheses apply to the high-resolution shell.

^b $R = \frac{\sum_h |F(h)_{obs} - F(h)_{calc}|}{\sum_h |F(h)_{obs}|}$ and $R_{meas} = \frac{[\sum_h N_h / (N_h - 1) \sum_i |I_i - \langle I \rangle|]}{\sum_h \sum_i I_i}$, where N_h is multiplicity for each reflection, I_i is the intensity of the i th observation of reflection h , and $\langle I \rangle$ is the mean intensity of all observations of reflection h , with $I_{\pm} = 1/N_h \sum_i I_i (-)$ or $I_i (+)$. \sum_i is taken over all reflections or is taken over all observations of each reflection. R_{cryst} and R_{free} were calculated using the working and test hkl reflection sets, respectively.

^c Calculated with Phenix get_cc_mtz_pdb (39).

^d Calculated with Mol Probity (62).

recognized as the Zn1 and Zn2 ions. The Zn-Zn distance (3.5 and 3.8 Å in chains A and B, respectively) is similar to that found in other dinuclear B3 lactamases (20–24). Zn1 is coordinated by the Nδ1 atom of residues His100 (118), His175 (196) Nε2, and Gln98 (116) Oε1 and a Zn-Zn bridging water molecule. The Zn1-Oε1(Gln) distance is 2.0 Å, pinpointing Gln98 (116) as a novel metal-binding residue in MBLs. On the other hand, Zn2 is coordinated to His103 (121) and His241 (263) Nε2, Asp102 (120)

Oδ2, and the bridging water molecule, adopting a distorted tetrahedral geometry. However, in all B3 lactamases crystallized so far, the coordination sphere in the Zn2 site adopts a trigonal bipyramidal geometry with two water ligands (20–24). The presence of additional nonprotein ligands in the GOB-18 site cannot be ruled out, given our data's resolution limit. Along the same line of thought, an axial water molecule with high mobility was modeled in the coordination sphere of the Zn1 ion in both GOB-18 monomers, but a larger species (such as glycerol from the cryoprotection solution) cannot be excluded.

The conformation of the zinc ligands in the GOB-18 active site is stabilized by a network of hydrogen bonds (Fig. 4B) involving outer sphere ligands. His100 (118) Nε2 and His175 (196) Nδ1 interact with Asp135 (153) and Ser202 (223) side chains, respectively, and Gln98 (116) Nε2 establishes contacts with Asn199 (220) Oδ1. Additionally, the Nδ1 atom of His103 (121) is H bonded with the main-chain N of residues Thr68 (85) and Gly69 (86) through a bridging water, His241 (263) Nε2 interacts with the side chain of Asp51 (67), and the carboxylate of Asp102 (120) contacts its own amide nitrogen. Most of these outer sphere ligands are conserved in B3 enzymes (20–24), despite the divergence introduced by the His116Gln replacement.

A novel feature in GOB-18 can be observed at residue Cys180 (201): its thiol and amide nitrogen make H bonds with the backbone carbonyls of Leu96 (114) and Thr97 (115), respectively (Fig. 3A). These residues are located in the β5-α3 loop, which contains the metal-binding motif Q₁₁₆XH₁₁₈XD₁₂₀H₁₂₁ that replaces the HXHXDH signature present in the rest of the B3 enzymes. Thus, Cys180 (201), within the β-strand just downstream from the loop including metal-binding His175 (196), connects the bases of two loops that comprise five out of six metal ligands and all the Zn1-coordinating residues.

The residues that define the substrate binding cleft in GOB-18 are found mainly in loops. The catalytic pocket (Fig. 5) is delimited by segments 23 to 32 (30 to 39) (spanning a nonstructured coil and a short, kinked helix), 51 to 52 (67 to 68), 98 to 103 (116 to 121) (including the QXHXDH motif), 135 to 144 (154 to 163) (encompassing a short helix), 175 to 176 (196 to 197) (containing metal-binding His175 [196]), 199 to 204 (220 to 225) (harboring residue Met 200 [221]), and 240 to 244 (262 to 266) (spanning a short helix and including metal-binding His241 [263]). This cleft, albeit shallow, is one of the top ranking cavities, comprising 150 to 200 Å³ with an opening of approximately 8 Å by 15 Å and 10 Å deep. A second, smaller pocket, with residues Ser202 (223), Gln244 (266), Asn271 (293), and Leu275 (297) conforming the side limits and Met200 (221) and Trp237 (259) on the floor, is immediately adjacent to the first one, constituting a discontinuous groove. Figure 5 compares the catalytic groove of GOB-18 to those from the B3 lactamases FEZ-1, L1, and BJP-1. The wide substrate-binding groove in GOB enzymes correlates with high catalytic efficiencies for a broad spectrum of substrates, in contrast to BJP-1, in which an N-terminal helix partially covers the active site (22).

Substrate docking and molecular dynamics simulations. We attempted to obtain a model for di-Zn(II) GOB-18 complexed with imipenem by *in silico* docking calculations. However, none of the resulting models reproduced binding modes consistent with a productive Michaelis complex. Similar docking simulations with L1 were instead successful, yielding a model which reproduced most of the binding features reported in the crystal structure of L1

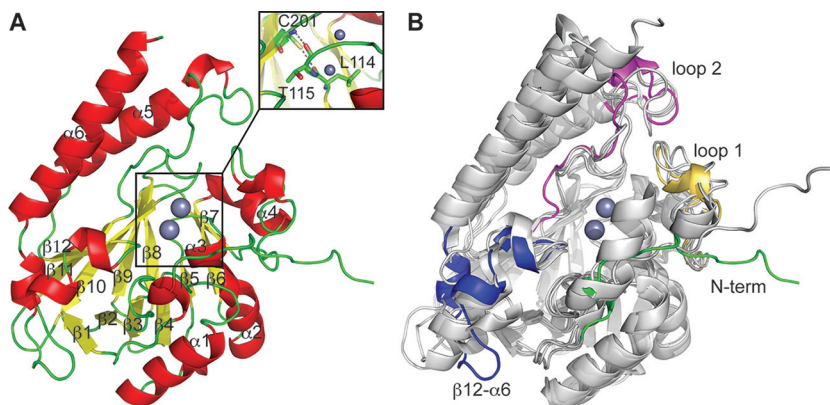


FIG 3 Overall structure of periplasmic GOB-18. (A) Cartoon representation of GOB-18 (chain A) with helices colored in red, strands in yellow, and nonstructured loops in green. The inset highlights selected residues (in stick representation). Dashed lines represent atomic interactions. (B) Comparison of GOB-18 with the B3 MBLs FEZ-1 (PDB entry 1K07), BJP-1 (PDB entry 3LVZ), and L1 (PDB entry 1SML). The segments of GOB-18 exhibiting the highest RMSD values are highlighted in different colors. Zn atoms are shown as gray spheres. N-term, N terminus.

in complex with hydrolyzed moxalactam (PDB entry 2A1O) (52) (see Fig. S1 in the supplemental material). In our docking model, the carbonyl C7 from imipenem is positioned close to the bridging OH^- enabling the nucleophilic attack, and the carboxylate C9 interacts with the Zn2 ion, anchoring the substrate, in agreement with the generally accepted productive binding mode of β -lactam compounds to dinuclear MBLs. Based on these results, we generated a model of GOB-18 in complex with imipenem by structural alignment of GOB-18 onto the L1-imipenem complex.

The L1-imipenem and GOB-18-imipenem models were used as starting geometries for molecular dynamics simulations and run for 50 ns. In the L1-imipenem complex, residues Ser221 and Ser223 interact with the carboxylate C9 of imipenem throughout the simulation (Fig. 6A). Additionally, the OH group C10 of imipenem established a hydrogen bond with the nonchelating oxygen of the Zn2-ligand Asp120. In GOB-18, Ser221 is replaced by a Met residue whose side chain points out of the active site, buried in the hydrophobic core of the protein; hence, it is unable to interact with the substrate (Fig. 6B). This orientation is conserved throughout the dynamics. On the other hand, the imipenem carboxylate contacts residue Ser202 (223) through a water molecule, and the interaction of the OH group C10 with Asp102 (120) is also preserved in the GOB-18-imipenem complex. Taken together, these data strongly suggest that the Ser221Met substitution has an impact on substrate binding by GOB enzymes.

The mobility of active-site loops in MBLs has been related to substrate specificity. Indeed, residues 221 and 223 are located in a loop flanking the active site (see Fig. S2 in the supplemental material). We calculated the fluctuations of residues within this loop in GOB-18 and L1, both in the resting state and in the Michaelis complex with imipenem. The RMSF of this loop is substantially larger in GOB-18 than in L1 (see Fig. S2). We propose that the Ser221Met substitution present in GOB enzymes is compensated for by a larger flexibility in this loop, which might assist substrate binding within the catalytic groove.

DISCUSSION

Here, we report the crystal structure and biochemical characterization of the periplasmic di-Zn(II) form of GOB-18 from *E. meningoseptica*. The structural data reveal that a Gln residue replaces

the ubiquitous His116 in the coordination sphere of the Zn1 ion (Fig. 4). Periplasmic GOB-18 is a fully active broad-spectrum lactamase in the di-Zn(II) form (Table 1), in agreement with a previous report that studied GOB-1 (30). These results contrast with our previous study with recombinant GOB-18 obtained from the cytoplasm of *E. coli* cells (29). In that case, accumulation of the protein in the bacterial cytoplasm resulted in an inactive Fe(III)-bound form, which could be demetallated and subsequently loaded with Zn(II) *in vitro* to obtain an active mono-Zn(II) variant. Indeed, the preferential binding of a given divalent cation over others is influenced by the cellular localization of proteins (53), and mismetallation upon protein overproduction in the cytoplasm of *E. coli* has been documented for a number of systems (54–56). Thus, these separate preparations give us the opportunity to compare mono- and di-Zn(II) variants of GOB-18.

We now show that when secreted into the bacterial periplasm, GOB exclusively binds Zn(II), which is relevant given that this is the physiological cellular compartment of MBLs in Gram-negative bacteria (53). Thus, in order to avoid chelation and remetallation steps, we optimized a protocol for the production of GOB-18 in the periplasm of *E. coli* and the preparation of large amounts of pure mature protein in the absence of affinity tags. Indeed, periplasmic GOB-18 preparations containing exclusively Zn(II) were successfully obtained, and while all efforts aimed at crystallizing the cytoplasmic Fe(III)-containing variant or the reconstituted mono-Zn(II) form of GOB-18 were unsuccessful, diffraction-quality crystals readily grew from solutions of periplasmic di-Zn(II) GOB-18. These results clearly show that the differences in metal content previously noted between GOB-1 and GOB-18 were due to the procedures employed to produce the recombinant proteins in each case and not due to the few residues differing in their primary structures. Taking all these data into account, it is safe to extrapolate several of the present conclusions to all GOB enzymes.

Periplasmic di-Zn(II) GOB-18 catalyzed hydrolysis of β -lactam substrates with k_{cat} and K_m values similar to those reported for mono-Zn(II)-GOB-18 and di-Zn(II)-GOB-1 (Table 1). In addition, previous analyses of mutant GOB-18 Asp120Ser and metal-substituted GOB-18 derivatives showed that the Zn2 site is essential for catalysis and for the stabilization of an anionic intermediate in the

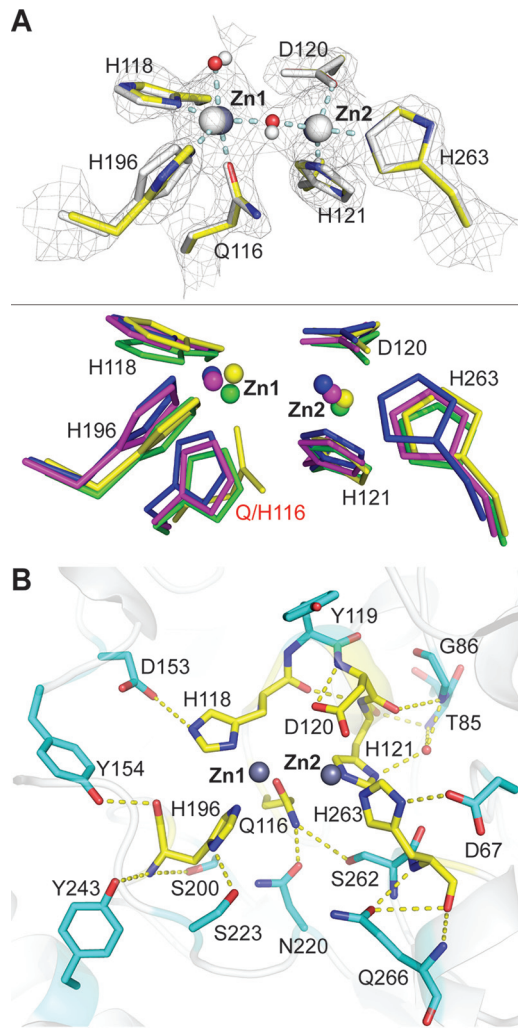


FIG 4 Active site of periplasmic GOB-18. (A, upper) Comparison of the active site in the two monomers present in the crystal structure of GOB-18. Chain A is colored by atom in yellow (C atoms), blue (N atoms), red (oxygen atoms), and dark gray (zinc atoms). Chain B is shown in light gray throughout. Protein residues are depicted as sticks, zinc atoms are shown as big spheres, and water molecules are small spheres. The 2mFo-DFc sigmaA-weighted electron density, contoured at 1.7 σ and represented as a gray mesh, corresponds to chain A. Dashed lines represent atomic interactions, and the related distances are 2.1 Å in all cases, except for the Zn1-Gln98 and Zn1-axial water interactions, where distances are 2.0 Å and 2.2 Å, respectively. (Lower) Comparison of the active site of GOB-18 (chain A, yellow) with those of the B3 MBLs FEZ-1 (PDB entry 1K07; pink), BJP-1 (PDB entry 3LVZ; green), and L1 (PDB entry 1SML; blue). (B) Residues in the second coordination sphere in the active site of GOB-18 (chain A) are shown in stick representation with C atoms colored in cyan.

hydrolysis of nitrocefim (29, 57). On the other hand, even though replacement of Gln116 by an isosteric His residue was somewhat detrimental for the resistance profile conferred by GOB-18 (29, 31), it had little effect on metal content or on the *in vitro* activity of dinuclear GOB-1 (30) and remetalated mono-Zn(II) GOB-18 (29). Indeed, mutations Gln116Asn and Gln116Ala, which are predicted to impact the structure of the Zn2 site through perturbations on the second coordination sphere (Fig. 4B), reduced the catalytic efficiency of GOB-1 (30). Overall, the available data indicate that the Zn1 site in GOB enzymes contributes only marginally to activity, whereas it may be critical for enzyme function *in*

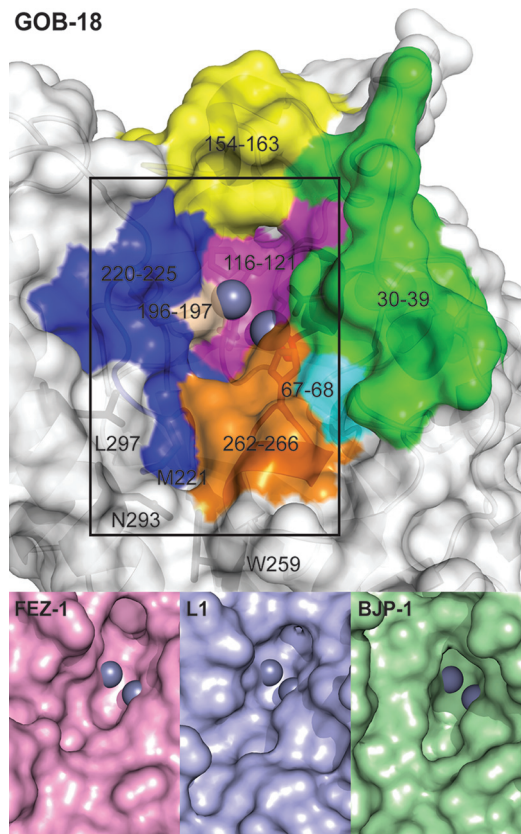


FIG 5 Catalytic groove in GOB-18. Surface representation of GOB-18 (chain A), with different colors highlighting the structural elements that define the catalytic groove. Zinc atoms are shown as gray spheres. For comparison, the region delimited by the rectangle is compared to the equivalent regions of the B3 MBLs FEZ-1 (PDB entry 1K07), L1 (PDB entry 1SML), and BJP-1 (PDB entry 3LVZ) shown at the bottom.

in vivo. This would depend on the zinc availability, which can vary widely depending on environmental conditions (8).

The finding of a dinuclear Zn(II) site where Gln116 acts as a metal ligand of the Zn1 ion contrasts with that found in B2 MBLs, where replacement of His116 by an Asn residue leads to a dinuclear nonactive species (18, 19). In the case of di-Zn(II)-Cpha, residue Asn116 does not act as a metal ligand and the Zn1 ion is coordinated by only two protein residues, adopting a nonproductive position (16). Instead, the longer side chain of Gln116 (isosteric to a His residue) in GOB enzymes makes it a good metal ligand, so that the Zn1 ion adopts a position similar to that held in other di-Zn MBLs (Fig. 7). The finding of a conserved network of hydrogen bonds among second-sphere ligands confirms the requirement of a similar geometric arrangement in the active site. We have also found that a unique Cys residue may help to anchor the two loops that provide protein ligands for the Zn1 ion (Fig. 3A). A conservative mutation of this Cys residue to a Ser (29) preserves the enzyme activity, supporting this hypothesis. The role of the Zn1 site in MBLs is to facilitate deprotonation of the bound water to provide an active nucleophile (1). This function cannot be properly fulfilled by the Zn1 ion in B2 enzymes, resulting in enzyme inhibition (16), but instead is fully preserved in GOB enzymes. Therefore, the His116Gln mutation is conservative in terms of both structure and function. The role of the Zn2 site is

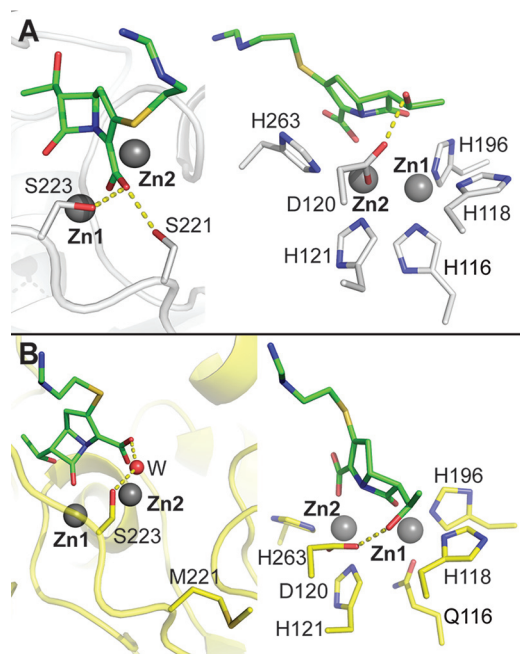


FIG 6 Molecular dynamics simulations calculated using *in silico* docked imipenem in complex with L1 and GOB-18. (A) Snapshot of the L1-imipenem molecular dynamics simulation showing the interaction between imipenem and residues Asp120, Ser221, and Ser223. (B) Snapshot of the GOB-18-imipenem molecular dynamics simulation showing the interaction between imipenem and residues Asp120 and Ser223. Imipenem is shown in stick representation with green carbons, L1 and GOB-18 are displayed in gray and yellow, respectively, and zinc atoms and a water molecule are depicted as gray and red spheres, respectively.

2-fold: to provide an anchoring electrostatic point for substrate binding and to stabilize the development of negative charge in the bridgehead nitrogen. Both functions also depend on the adequate positioning of this metal ion, which is indeed maintained in GOB-18.

Position 221 is essential in B1 and B2 MBLs, where a Cys residue acts as a ligand of the Zn2 ion. Instead, in most B3 enzymes a Ser is found in this position. The report of a Met residue in position 221 in GOB enzymes led us to speculate that the thioether moiety acts as a weak metal ligand. However, mutagenesis experiments in GOB-18 showed that Met221 is not involved in metal binding or in catalysis but instead has a structural role (31, 32). The crystal structure that we are now disclosing confirms that Met221 is not a metal ligand; actually, its side chain does not point toward the substrate-binding site (Fig. 6). In addition, docking and molecular dynamics simulations confirm that this residue is not involved in substrate binding, in sharp contrast to the role of the conserved Ser221 in most B3 enzymes. Therefore, these results provide the first available evidence for an MBL where residue 221 is not involved in metal chelation or in substrate binding and highlight the diversity of roles fulfilled by this position among enzymes within the family. Additionally, a wide substrate-binding groove in GOB-18 (Fig. 5) correlates with a high catalytic efficiency against a diverse range of β -lactam substrates (Table 1) compared to other B3 MBLs, in agreement with previous observations.

The metal binding site of GOB enzymes is unusual not only

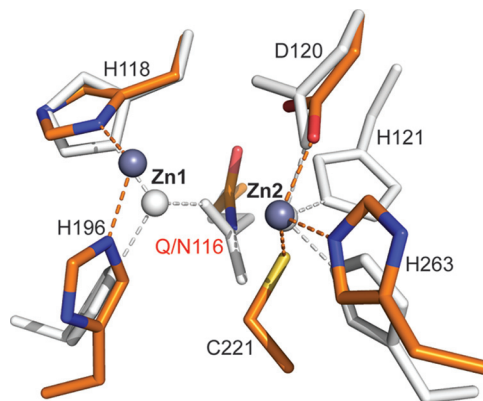


FIG 7 Comparison of the active sites of di-Zn(II) GOB-18 and di-Zn(II) CphA. GOB-18 (chain A) is shown in light gray, and CphA (PDB entry 3F9O) is colored in orange (C atoms), blue (N atoms), red (oxygen atoms), and dark gray (zinc atoms). Protein residues are shown as sticks, zinc atoms are depicted as spheres, and dashed lines highlight atomic interactions.

among MBLs. Indeed, Asn/Gln ligands in protein zinc sites are very rare (0.5% of the cases according to Dudev et al.) (58). Surprisingly, the His116Gln substitution does not have a direct impact on the broad-spectrum profile of GOB-18. GOB is also peculiar in that its native organism, *E. meningoseptica*, is the only known bacterium expressing two MBLs: the B1 enzyme BlaB and the B3 enzyme GOB. We have shown that even if both genes are actively expressed, the higher levels of BlaB make this enzyme the one responsible for carbapenemase resistance (33). Thus, GOB could be redundant in this organism despite its efficient catalytic performance. GOB-like alleles have also been found in metagenomics studies of a remote Alaskan soil with minimal human-induced selective pressure (59). More recently, new MBLs closely homologous to GOB enzymes have been found in *Pedobacter roseus* (PEDO-1), *Pedobacter borealis* (PEDO-2), *Chryseobacterium piscium* (CPS-1), and *Epilithonimonas tenax* (ESP-1) (60, 61). All these MBLs feature the characteristic Gln116 residue in the active site, the Cys residue in the second-sphere position, and a hydrophobic residue in position 221 (Met or Leu), as discussed for the present crystal structure, confirming that GOB-like alleles are ubiquitous in environmental bacteria. We speculate that GOB genes serve as a rather ancient resistance reservoir or give rise to a different, unknown function elicited by the presence of the Gln residue, providing at the same time an independent source of antibiotic resistance. In any case, these findings further highlight the large structural diversity of MBLs in current microorganisms, the details of which constitute valuable information in conceiving better antibiotic design strategies.

ACKNOWLEDGMENTS

We thank R. Girolami for atomic absorption measurements.

M.-N.L. is a postdoctoral fellow from ANII and was a recipient of a doctoral fellowship from CONICET. S.I.D. is the recipient of a doctoral fellowship from CONICET. J.M.-B., D.M.M., A.M.V., and A.J.V. are staff members from CONICET. This work was supported by grants from ANPCyT and the U.S. National Institutes of Health (1R01AI100560) to A.J.V., from ANPCyT, CONICET, UNR, and Ministerio de Salud, Provincia de Santa Fe, Argentina, to A.M.V., and from ANPCyT and CONICET to D.M.M.

FUNDING INFORMATION

This work, including the efforts of Alejandro J. Vila, was funded by HHS | National Institutes of Health (NIH) (1R01AI100560).

This work was supported by grants from ANPCyT and the U.S. National Institutes of Health (1R01AI100560) to A.J.V., from ANPCyT, CONICET, UNR, and Ministerio de Salud, Provincia de Santa Fe, Argentina, to A.M.V., and from ANPCyT and CONICET to D.M.M.

REFERENCES

- Meini MR, Llarrull LI, Vila AJ. 2015. Overcoming differences: the catalytic mechanism of metallo-beta-lactamases. *FEBS Lett* 589:3419–3432. <http://dx.doi.org/10.1016/j.febslet.2015.08.015>.
- Meini MR, Llarrull LI, Vila AJ. 2014. Evolution of metallo-beta-lactamases: trends revealed by natural diversity and in vitro evolution. *Antibiotics (Basel)* 3:285–316. <http://dx.doi.org/10.3390/antibiotics3030285>.
- Palzkill T. 2013. Metallo-beta-lactamase structure and function. *Ann N Y Acad Sci* 1277:91–104. <http://dx.doi.org/10.1111/j.1749-6632.2012.06796.x>.
- Llarrull LI, Testero SA, Fisher JF, Mobashery S. 2010. The future of the beta-lactams. *Curr Opin Microbiol* 13:551–557. <http://dx.doi.org/10.1016/j.mib.2010.09.008>.
- Fisher JF, Meroueh SO, Mobashery S. 2005. Bacterial resistance to beta-lactam antibiotics: compelling opportunism, compelling opportunity. *Chem Rev* 105:395–424. <http://dx.doi.org/10.1021/cr030102i>.
- Crowder MW, Spencer J, Vila AJ. 2006. Metallo-beta-lactamases: novel weaponry for antibiotic resistance in bacteria. *Acc Chem Res* 39:721–728. <http://dx.doi.org/10.1021/ar0400241>.
- Galleni M, Lamotte-Brasseur J, Rossolini GM, Spencer J, Dideberg O, Frere JM. 2001. Standard numbering scheme for class B beta-lactamases. *Antimicrob Agents Chemother* 45:660–663. <http://dx.doi.org/10.1128/AAC.45.3.660-663.2001>.
- Gonzalez JM, Meini MR, Tomatis PE, Martin FJ, Cricco JA, Vila AJ. 2012. Metallo-beta-lactamases withstand low Zn(II) conditions by tuning metal-ligand interactions. *Nat Chem Biol* 8:698–700.
- Llarrull LI, Tioni MF, Vila AJ. 2008. Metal content and localization during turnover in *B. cereus* metallo-beta-lactamase. *J Am Chem Soc* 130:15842–15851. <http://dx.doi.org/10.1021/ja801168r>.
- Hawk MJ, Breece RM, Hajdin CE, Bender KM, Hu Z, Costello AL, Bennett B, Tierney DL, Crowder MW. 2009. Differential binding of Co(II) and Zn(II) to metallo-beta-lactamase Bla2 from *Bacillus anthracis*. *J Am Chem Soc* 131:10753–10762. <http://dx.doi.org/10.1021/ja900296u>.
- Fabiane SM, Sohi MK, Wan T, Payne DJ, Bateson JH, Mitchell T, Sutton BJ. 1998. Crystal structure of the zinc-dependent beta lactamase from *Bacillus cereus* at 1.9 Å resolution: binuclear active site with features of a mononuclear enzyme. *Biochemistry* 37:12404–12411. <http://dx.doi.org/10.1021/bi980506i>.
- Garcia-Saez I, Docquier JD, Rossolini GM, Dideberg O. 2008. The three-dimensional structure of VIM-2, a Zn-beta-lactamase from *Pseudomonas aeruginosa* in its reduced and oxidized form. *J Mol Biol* 375:604–611. <http://dx.doi.org/10.1016/j.jmb.2007.11.012>.
- Concha N, Rasmussen BA, Bush K, Herzberg O. 1996. Crystal structure of the wide-spectrum binuclear zinc beta-lactamase from *Bacteroides fragilis*. *Structure* 4:823–836. [http://dx.doi.org/10.1016/S0969-2126\(96\)00089-5](http://dx.doi.org/10.1016/S0969-2126(96)00089-5).
- King DT, Worrall LJ, Gruninger R, Strynadka NC. 2012. New Delhi metallo-beta-lactamase: structural insights into beta-lactam recognition and inhibition. *J Am Chem Soc* 134:11362–11365. <http://dx.doi.org/10.1021/ja303579d>.
- Gonzalez LJ, Moreno DM, Bonomo RA, Vila AJ. 2014. Host-specific enzyme-substrate interactions in SPM-1 metallo-beta-lactamase are modulated by second sphere residues. *PLoS Pathog* 10:e1003817. <http://dx.doi.org/10.1371/journal.ppat.1003817>.
- Bebrone C, Delbruck H, Kupper MB, Schlomer P, Willmann C, Frere JM, Fischer R, Galleni M, Hoffmann KM. 2009. The structure of the dizinc subclass B2 metallo-beta-lactamase CphA reveals that the second inhibitory zinc ion binds in the histidine site. *Antimicrob Agents Chemother* 53:4464–4471. <http://dx.doi.org/10.1128/AAC.00288-09>.
- Hernandez Valladares M, Felici A, Weber G, Adolph HW, Zeppezauer M, Rossolini GM, Amicosante G, Frere JM, Galleni M. 1997. Zn(II) dependence of the *Aeromonas hydrophila* AE036 metallo-beta-lactamase activity and stability. *Biochemistry* 36:11534–11541. <http://dx.doi.org/10.1021/bi971056h>.
- Fonseca F, Bromley EH, Saavedra MJ, Correia A, Spencer J. 2011. Crystal structure of *Serratia fonticola* Sfh-1: activation of the nucleophile in mono-zinc metallo-beta-lactamases. *J Mol Biol* 411:951–959. <http://dx.doi.org/10.1016/j.jmb.2011.06.043>.
- Garau G, Bebrone C, Anne C, Galleni M, Frere JM, Dideberg O. 2005. A metallo-beta-lactamase enzyme in action: crystal structures of the monozinc carbapenemase CphA and its complex with biapenem. *J Mol Biol* 345:785–795. <http://dx.doi.org/10.1016/j.jmb.2004.10.070>.
- Ullah JH, Walsh TR, Taylor IA, Emery DC, Verma CS, Gamblin SJ, Spencer J. 1998. The crystal structure of the L1 metallo-beta-lactamase from *Stenotrophomonas maltophilia* at 1.7 Å resolution. *J Mol Biol* 284:125–136. <http://dx.doi.org/10.1006/jmbi.1998.2148>.
- Garcia-Saez I, Mercuri PS, Papamicael C, Kahn R, Frere JM, Galleni M, Rossolini GM, Dideberg O. 2003. Three-dimensional structure of FEZ-1, a monomeric subclass B3 metallo-beta-lactamase from *Fluoribacter gormanii*, in native form and in complex with D-captopril. *J Mol Biol* 325:651–660. [http://dx.doi.org/10.1016/S0022-2836\(02\)01271-8](http://dx.doi.org/10.1016/S0022-2836(02)01271-8).
- Docquier JD, Benvenuti M, Calderone V, Stoczko M, Menciassi N, Rossolini GM, Mangani S. 2010. High-resolution crystal structure of the subclass B3 metallo-beta-lactamase BJP-1: rational basis for substrate specificity and interaction with sulfonamides. *Antimicrob Agents Chemother* 54:4343–4351. <http://dx.doi.org/10.1128/AAC.00409-10>.
- Wachino J, Yamaguchi Y, Mori S, Kurosaki H, Arakawa Y, Shibayama K. 2013. Structural insights into the subclass B3 metallo-beta-lactamase SMB-1 and the mode of inhibition by the common metallo-beta-lactamase inhibitor mercaptoacetate. *Antimicrob Agents Chemother* 57:101–109. <http://dx.doi.org/10.1128/AAC.01264-12>.
- Leiros HK, Borra PS, Brandsdal BO, Edvardsen KS, Spencer J, Walsh TR, Samuelsen O. 2012. Crystal structure of the mobile metallo-beta-lactamase AIM-1 from *Pseudomonas aeruginosa*: insights into antibiotic binding and the role of Gln157. *Antimicrob Agents Chemother* 56:4341–4353. <http://dx.doi.org/10.1128/AAC.00448-12>.
- Bellais S, Aubert D, Naas T, Nordmann P. 2000. Molecular and biochemical heterogeneity of class B carbapenem-hydrolyzing beta-lactamases in *Chryseobacterium meningosepticum*. *Antimicrob Agents Chemother* 44:1878–1886. <http://dx.doi.org/10.1128/AAC.44.7.1878-1886.2000>.
- Bloch KC, Nadarajah R, Jacobs R. 1997. *Chryseobacterium meningosepticum*: an emerging pathogen among immunocompromised adults. Report of 6 cases and literature review. *Medicine (Baltimore, MD)* 76:30–41.
- Lee SW, Tsai CA, Lee BJ. 2008. *Chryseobacterium meningosepticum* sepsis complicated with retroperitoneal hematoma and pleural effusion in a diabetic patient. *J Chin Med Assoc* 71:473–476. [http://dx.doi.org/10.1016/S1726-4901\(08\)70151-5](http://dx.doi.org/10.1016/S1726-4901(08)70151-5).
- Shinha T, Ahuja R. 2015. Bacteremia due to *Elizabethkingia meningoseptica*. *ID Cases* 2:13–15.
- Moran-Barrio J, Gonzalez JM, Lisa MN, Costello AL, Peraro MD, Carloni P, Bennett B, Tierney DL, Limansky AS, Viale AM, Vila AJ. 2007. The metallo-beta-lactamase GOB is a mono-Zn(II) enzyme with a novel active site. *J Biol Chem* 282:18286–18293. <http://dx.doi.org/10.1074/jbc.M700467200>.
- Horsfall LE, Izougarhane Y, Lassaux P, Selevsek N, Lienard BM, Poirel L, Kupper MB, Hoffmann KM, Frere JM, Galleni M, Bebrone C. 2011. Broad antibiotic resistance profile of the subclass B3 metallo-beta-lactamase GOB-1, a di-zinc enzyme. *FEBS J* 278:1252–1263. <http://dx.doi.org/10.1111/j.1742-4658.2011.08046.x>.
- Moran-Barrio J, Lisa MN, Vila AJ. 2012. In vivo impact of Met221 substitution in GOB metallo-beta-lactamase. *Antimicrob Agents Chemother* 56:1769–1773. <http://dx.doi.org/10.1128/AAC.05418-11>.
- Lisa MN, Moran-Barrio J, Guindon MF, Vila AJ. 2012. Probing the role of Met221 in the unusual metallo-beta-lactamase GOB-18. *Inorg Chem* 51:12419–12425.
- Gonzalez LJ, Vila AJ. 2012. Carbapenem resistance in *Elizabethkingia meningoseptica* is mediated by metallo-beta-lactamase BlaB. *Antimicrob Agents Chemother* 56:1686–1692. <http://dx.doi.org/10.1128/AAC.05835-11>.
- Kabsch W. 2010. XDS. *Acta Crystallogr D Biol Crystallogr* 66:125–132. <http://dx.doi.org/10.1107/S0907444909047337>.
- Winn MD, Ballard CC, Cowtan KD, Dodson EJ, Emsley P, Evans PR, Keegan RN, Krissinel EB, Leslie AGW, McCoy A, McNicholas SJ, Murshudov GM, Pannu NS, Potterton EA, Powell HR, Read RJ, Vagin A, Wilson KS. 2011. Overview of the CCP4 suite and current develop-

- ments. *Acta Crystallogr D Biol Crystallogr* 67:235–242. <http://dx.doi.org/10.1107/S0907444910045749>.
36. McCoy AJ, Grosse-Kunstleve RW, Adams PD, Winn MD, Storoni LC, Read RJ. 2007. Phaser crystallographic software. *J Appl Crystallogr* 40: 658–674. <http://dx.doi.org/10.1107/S0021889807021206>.
 37. Emsley P, Lohkamp B, Scott WG, Cowtan K. 2010. Features and development of Coot. *Acta Crystallogr D Biol Crystallogr* 66:486–501. <http://dx.doi.org/10.1107/S0907444910007493>.
 38. Bricogne G, Blanc E, Brandl M, Flensburg C, Keller P, Paciorek W, Roversi P, Sharff A, Smart OS, Vornrhein C, Womack TO. 2011. BUSTER version 2.11.4. Global Phasing Ltd., Cambridge, United Kingdom.
 39. Adams PD, Grosse-Kunstleve RW, Hung LW, Ioerger TR, McCoy AJ, Moriarty NW, Read RJ, Sacchettini JC, Sauter NK, Terwilliger TC. 2002. PHENIX: building new software for automated crystallographic structure determination. *Acta Crystallogr D Biol Crystallogr* 58:1948–1954. <http://dx.doi.org/10.1107/S0907444902016657>.
 40. Dundas J, Ouyang Z, Tseng J, Binkowski A, Turpaz Y, Liang J. 2006. CASTp: computed atlas of surface topography of proteins with structural and topographical mapping of functionally annotated residues. *Nucleic Acids Res* 34:W116–W118. <http://dx.doi.org/10.1093/nar/gkl282>.
 41. Laurie AT, Jackson RM. 2005. Q-SiteFinder: an energy-based method for the prediction of protein-ligand binding sites. *Bioinformatics* 21:1908–1916. <http://dx.doi.org/10.1093/bioinformatics/bti315>.
 42. Morris GM, Huey R, Lindstrom W, Sanner MF, Belew RK, Goodsell DS, Olson AJ. 2009. AutoDock4 and AutoDockTools4: automated docking with selective receptor flexibility. *J Comput Chem* 30:2785–2791. <http://dx.doi.org/10.1002/jcc.21256>.
 43. Humphrey W, Dalke A, Schulten K. 1996. VMD: visual molecular dynamics. *J Mol Graph* 14:33–38. [http://dx.doi.org/10.1016/0263-7855\(96\)00018-5](http://dx.doi.org/10.1016/0263-7855(96)00018-5).
 44. Jorgensen WL, Chandrasekhar J, Madura JD, Impey RW, Klein ML. 1983. Comparison of simple potential functions for simulating liquid water. *J Chem Phys* 79:926. <http://dx.doi.org/10.1063/1.445869>.
 45. Pearlman DA, Case DA, Caldwell JW, Ross WS, Cheatham TE, DeBolt S, Ferguson D, Seiblen G, Kollman P. 1995. AMBER, a package of computer programs for applying molecular mechanics, normal mode analysis, molecular dynamics and free energy calculations to simulate the structural and energetic properties of molecules. *Comput Phys Commun* 91:1–41. [http://dx.doi.org/10.1016/0010-4655\(95\)00041-D](http://dx.doi.org/10.1016/0010-4655(95)00041-D).
 46. Case DA, Babin V, Berryman JT, Berz RM, Cai Q, Cerutti DS, Cheatham TE, III, Darden TA, Duke RE, Gohlke H, Goetz AW, Gusarov S, Homeyer N, Janowski P, Kaus J, Kolossvary I, Kovalenko A, Lee TS, LeGrand S, Luchko T, Luo R, Madej B, Merz KM, Paesani F, Roe DR, Roitberg A, Sagui C, Salomon-Ferrer R, Seabra G, Simmerling CL, Smith W, Swails J, Walker RC, Wang J, Wolf RM, Wu X, Kollman PA. 2014. AMBER 14. University of California, San Francisco, CA.
 47. Maier JA, Martinez C, Kasavajhala K, Wickstrom L, Hauser KE, Simmerling C. 2015. ff14SB: improving the accuracy of protein side chain and backbone parameters from ff99SB. *J Chem Theory Comput* 11:3696–3713. <http://dx.doi.org/10.1021/acs.jctc.5b00255>.
 48. Luty BA, Tironi IG, van Gunsteren WF. 1995. Lattice-sum methods for calculating electrostatic interactions in molecular simulation. *J Chem Phys* 103:3014. <http://dx.doi.org/10.1063/1.470490>.
 49. Berendsen HJC, Postma JPM, van Gunsteren WF, Dinola A, Haak JR. 1984. Molecular dynamics with coupling to an external bath. *J Chem Phys* 81:3684–3690. <http://dx.doi.org/10.1063/1.448118>.
 50. Ryckaert JP, Ciccotti G, Berendsen HJC. 1977. Numerical-integration of cartesian equations of motion of a system with constraints—molecular-dynamics of N-alkanes. *J Comput Phys* 23:327–341. [http://dx.doi.org/10.1016/0021-9991\(77\)90098-5](http://dx.doi.org/10.1016/0021-9991(77)90098-5).
 51. Roe DR, Cheatham TE, III. 2013. PTRAJ and CPPTRAJ: software for processing and analysis of molecular dynamics trajectory data. *J Chem Theory Comput* 9:3084–3095. <http://dx.doi.org/10.1021/ct400341p>.
 52. Spencer J, Read J, Sessions RB, Howell S, Blackburn GM, Gamblin SJ. 2005. Antibiotic recognition by binuclear metallo-beta-lactamases revealed by X-ray crystallography. *J Am Chem Soc* 127:14439–14444. <http://dx.doi.org/10.1021/ja0536062>.
 53. Moran-Barrio J, Limansky AS, Viale AM. 2009. Secretion of GOB metallo-beta-lactamase in *Escherichia coli* depends strictly on the cooperation between the cytoplasmic DnaK chaperone system and the Sec machinery: completion of folding and Zn(II) ion acquisition occur in the bacterial periplasm. *Antimicrob Agents Chemother* 53:2908–2917. <http://dx.doi.org/10.1128/AAC.01637-08>.
 54. Tottey S, Waldron KJ, Firbank SJ, Reale B, Bessant C, Sato K, Cheek TR, Gray J, Banfield MJ, Dennison C, Robinson NJ. 2008. Protein-folding location can regulate manganese-binding versus copper- or zinc-binding. *Nature* 455:1138–1142. <http://dx.doi.org/10.1038/nature07340>.
 55. Nar H, Huber R, Messerschmidt A, Filippou AC, Barth M, Jaquinod M, van de Kamp M, Canters GW. 1992. Characterization and crystal structure of zinc azurin, a by-product of heterologous expression in *Escherichia coli* of *Pseudomonas aeruginosa* copper azurin. *Eur J Biochem* 205:1123–1129. <http://dx.doi.org/10.1111/j.1432-1033.1992.tb16881.x>.
 56. Cotruvo JA, Jr, Stubbe J. 2012. Metallation and mismetallation of iron and manganese proteins in vitro and in vivo: the class I ribonucleotide reductases as a case study. *Metallomics* 4:1020–1036. <http://dx.doi.org/10.1039/c2mt20142a>.
 57. Lisa MN, Hemmingsen L, Vila AJ. 2010. Catalytic role of the metal ion in the metallo-beta-lactamase GOB. *J Biol Chem* 285:4570–4577. <http://dx.doi.org/10.1074/jbc.M109.063743>.
 58. Dudev T, Lin YL, Dudev M, Lim C. 2003. First-second shell interactions in metal binding sites in proteins: a PDB survey and DFT/CDM calculations. *J Am Chem Soc* 125:3168–3180. <http://dx.doi.org/10.1021/ja0209722>.
 59. Allen HK, Moe LA, Rodbumrer J, Gaarder A, Handelsman J. 2009. Functional metagenomics reveals diverse beta-lactamases in a remote Alaskan soil. *ISME J* 3:243–251. <http://dx.doi.org/10.1038/ismej.2008.86>.
 60. Gudeta DD, Pollini S, Docquier JD, Bortolaia V, Rossolini GM, Guardabassi L. 2016. Biochemical characterization of CPS-1, a subclass B3 metallo-beta-lactamase from a *Chryseobacterium piscium* soil isolate. *Antimicrob Agents Chemother* 60:1869–1873. <http://dx.doi.org/10.1128/AAC.01924-15>.
 61. Gudeta DD, Bortolaia V, Amos G, Wellington EM, Brandt KK, Poirel L, Nielsen JB, Westh H, Guardabassi L. 2016. The soil microbiota harbors a diversity of carbapenem-hydrolyzing beta-lactamases of potential clinical relevance. *Antimicrob Agents Chemother* 60:151–160. <http://dx.doi.org/10.1128/AAC.01424-15>.
 62. Chen VB, Arendall WB, III, Headd JJ, Keedy DA, Immormino RM, Kapral GJ, Murray LW, Richardson JS, Richardson DC. 2010. MolProbity: all-atom structure validation for macromolecular crystallography. *Acta Crystallogr D Biol Crystallogr* 66:12–21. <http://dx.doi.org/10.1107/S0907444909042073>.